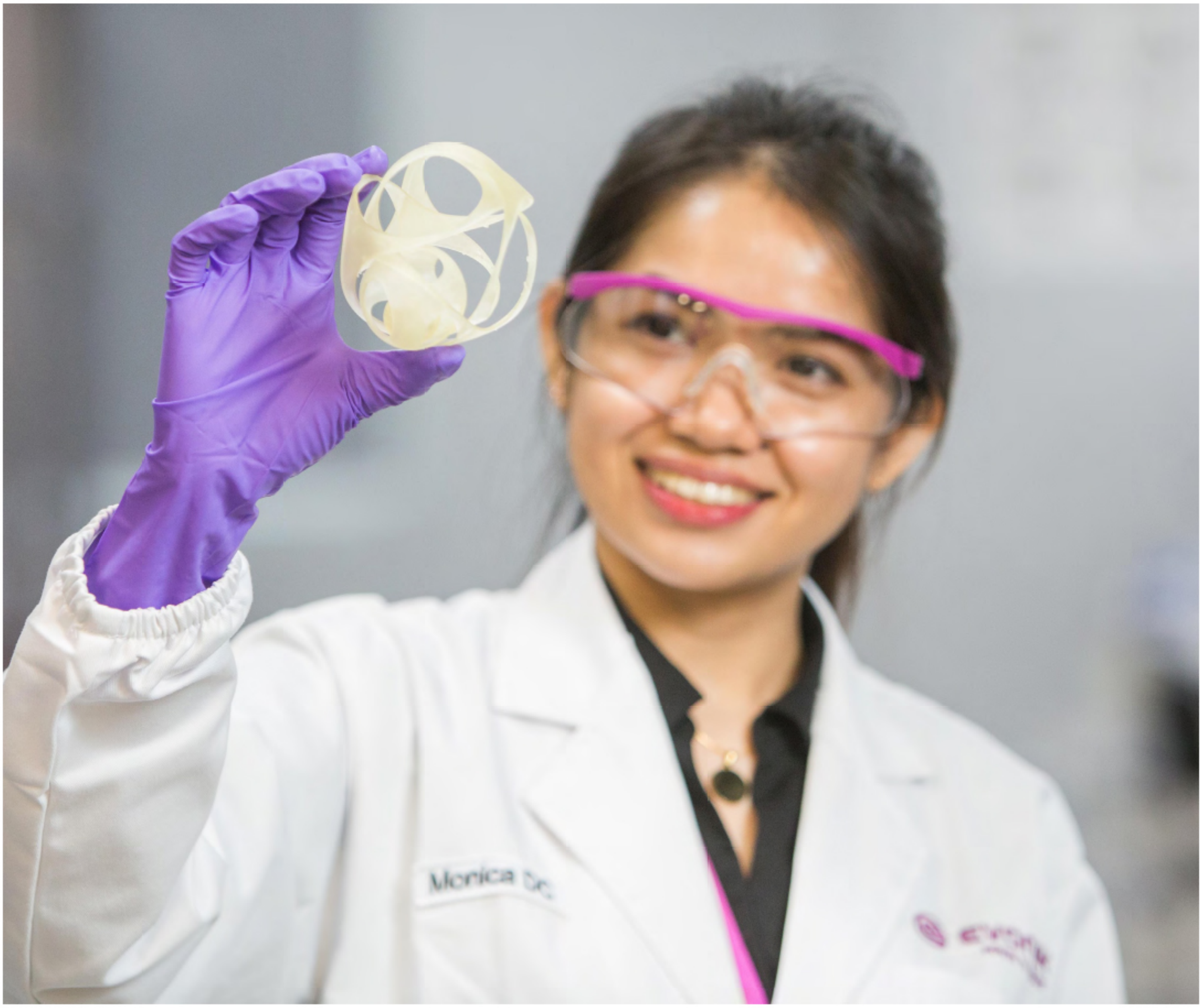

Pushing the boundaries of chemistry?
It takes
#HumanChemistry

Make your curiosity and talent as a chemist matter to the world with a specialty chemicals leader. Together, we combine cutting-edge science with engineering expertise to create solutions that answer real-world problems. Find out how our approach to technology creates more opportunities for growth, and see what chemistry can do for you at:

evonik.com/career

EVONIK
Leading Beyond Chemistry

ADVANCED FUNCTIONAL MATERIALS
www.afm-journal.de

Antisite Defects Stabilized by Antiphase Boundaries in $YFeO_3$ Thin Films

*Abinash Kumar, Konstantin Klyukin, Shuai Ning, Cigdem Ozsoy-Keskinbora, Mikhail Ovsyanko, Felix van Uden, Ruud Krijnen, Bilge Yildiz, Caroline A. Ross, and James M. LeBeau**

$YFeO_3$ thin films are a recent addition to the family of multiferroic orthoferrites where Y_{Fe} antisite defects and strain have been shown to introduce polar displacements while retaining magnetic properties. Complete control of the multiferroic properties, however, necessitates knowledge of the defects present and their potential role in modifying behavior. Here, the structure and chemistry of antiphase boundaries in Y-rich multiferroic $YFeO_3$ thin films are reported using aberration corrected scanning transmission electron microscopy combined with atomic resolution energy dispersive X-ray spectroscopy. It is found that Fe_Y antisites, which are not stable in the Y-rich film bulk, periodically arrange along antiphase boundaries due to changes in the local structural environment. Using density functional theory, it is shown that the antiphase boundaries are polar and bi-stable, where the presence of Fe_Y antisites significantly decreases the switching barrier. These results highlight how planar defects, such as antiphase boundaries, can stabilize point defects that would otherwise not be expected to form within the structure.

1. Introduction

While the orthoferrite $YFeO_3$ (YFO) is centrosymmetric (non-polar) and antiferromagnetic,[1,2] it exhibits multiferroic behavior when grown as a thin film under nominally stoichiometric and Y-rich conditions.[3] Specifically, the introduction of Y_{Fe} antisites breaks crystal inversion symmetry (Pbnm to $R3c$) and stabilizes a spontaneous dipole moment that leads to stoichiometry-dependent ferroelectricity. Although the resulting multiferroic behavior is robust, planar defects are also found in YFO thin films grown on $SrTiO_3$, which requires further investigation to gain complete control over the material properties.[4]

Planar defects, such as twins or antiphase boundaries (APBs), in the ferroic systems can modify both the local magnetic and polarization responses. Importantly, the behavior at the boundaries differ greatly from the rest of the material. For example, twins in $CaTiO_3$ have been shown to exhibit polar displacements that lead to local ferrielectricity.[5,6] Similarly, the presence of APBs in Fe_3O_4 reduces the total magnetization.[7] By controlling planar defect density during growth, either through substrate surface steps,[8–10] cation off-stoichiometry,[11] lattice symmetry mismatch between the thin film and substrate,[12] or strain,[13] the thin film properties can be tuned.[14,15]

The structure and chemistry of planar defects can also lead to the stabilization of otherwise unexpected point defects. Specifically, planar defects have been shown to modify the formation energy of point defects,[16] reducing the energy of those that may not occur in the "bulk". Because Y^{3+} and Fe^{3+} cations are isovalent in YFO, for example, Fe_Y and/or Y_{Fe} antisites could form without changes in stoichiometry. As determined with density functional theory, Fe_Y antisites in a thin film have a significantly higher formation energy than Y_{Fe} due to the atomic size mismatch ($r_Y = 106$ pm and $r_{Fe} = 65$ pm[17]).[3] The bonding environment for atoms at planar defects, however, is considerably different than the 'pristine' crystal and thus other types of point defects may be present in thin film YFO. This adds an additional 'knob' of property control through defect engineering.

Here, we determine the structure of APBs in multiferroic Y-rich $YFeO_3$ (YFO) thin films using aberration corrected scanning transmission electron microscopy (STEM). Via atomic resolution energy dispersive X-ray spectroscopy (EDS) acquired with a large solid angle of collection (>4 strad), we confirm that despite the Y-rich composition, the APBs host Fe_Y antisites that are not found elsewhere in the film. We also show that significant relaxation occurs at the APBs. Using the structure observed from STEM, we apply density functional theory (DFT) to show that the observed APBs have a low formation energy

---

A. Kumar, K. Klyukin, S. Ning,[+] B. Yildiz, C. A. Ross, J. M. LeBeau
Department of Materials Science and Engineering
Massachusetts Institute of Technology
Cambridge, MA 02139, USA
E-mail: lebeau@mit.edu

C. Ozsoy-Keskinbora, M. Ovsyanko, F. van Uden, R. Krijnen
Transmission Electron Microscopy Division
Thermo Fisher Scientific
Eindhoven 5651GG, Netherlands

B. Yildiz
Department of Nuclear Science and Engineering
Massachusetts Institute of Technology
Cambridge, MA 02139, USA

The ORCID identification number(s) for the author(s) of this article can be found under https://doi.org/10.1002/adfm.202107017.

[+]Present address: School of Materials Science and Engineering, Nankai University, Tianjin 300350, P. R. China

DOI: 10.1002/adfm.202107017

and exhibit a bi-stable polar distortion. We show that the Fe_Y antisite formation energy and polarization switching barrier are reduced by a factor of three at boundaries, leading to changes in local properties.

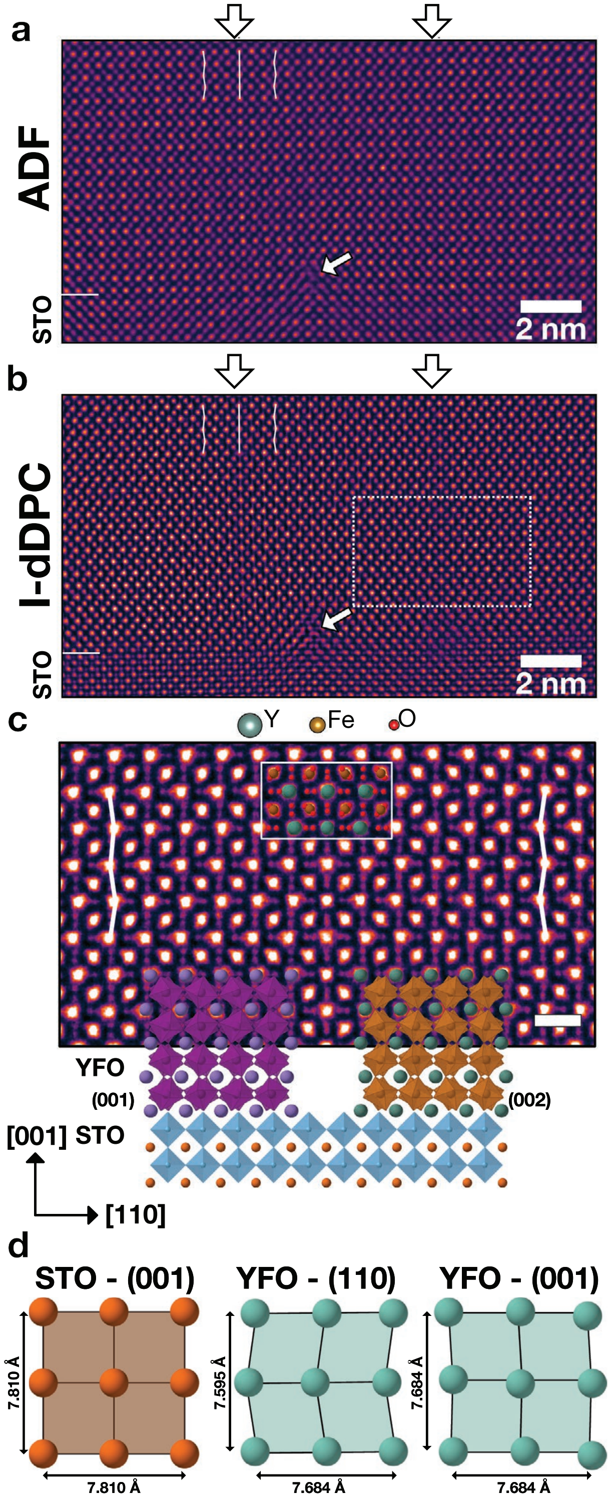

Figure 1. a) ADF and b) inverted dDPC (I-dDPC) STEM images of the Y-rich YFO thin film grown on Nb:STO. The horizontal lines at the left mark the film/substrate interface, while the arrows and chevrons indicate the positions of APBs. The arrows inside the figure indicate a misfit dislocation. c) An atomic resolution I-dDPC image highlighting the cation and anion positions across the APB, where the inset provides the DFT relaxed structure. The schematic shows that (110) APBs result when nuclei starting on different planes [(001) left and (002) right] grow together. The scale bar represents 500 pm. d) Schematic of the cation arrangement in the (001) of STO, and the (110) and (001) of YFO. The distances between the doubled pseudocubic perovskite unit cells are shown in each case.

2. Results and Discussion

The Y-rich multiferroic YFO thin films studied here are grown by pulsed laser deposition on Nb doped $SrTiO_3$ and are approximately 30 nm thick.[3] The Y:Fe ratio was 1.20 and the films showed a room temperature remanent polarization on the order of 10 $\mu C\ cm^{-2}$ and a saturation magnetization of 0.06 μ_B/f.u. arising from canted antiferromagnetic order. Compared with a cubic perovskite, the orthorhombic YFO unit cell with lattice parameters a = 5.587 Å, b = 5.274 Å and c = 7.5951 Å, is rotated by $\pi/4$ and doubled along the c axis. With a nominal misfit of –1.6%, the films exhibit an epitaxial relationship of $(001)_{YFO} \parallel (001)_{STO}$ and $[110]_{YFO} \parallel [100]_{STO}$ in-plane, where the YFO directions are given using the Pbnm spacegroup setting. The [001] of the film and substrate are parallel out-of-plane.

Using aberration corrected annular dark-field (ADF) and differentiated differential phase contrast (dDPC) STEM, **Figure 1**a,b, the substrate/film interface and defects can be identified. The STO substrate can be distinguished by the slight decrease in intensity in the lower sixth of both images. Two APBs, indicated by arrows at the top of Figure 1a,b, occur where the zigzagging of the Y atom columns is mirrored on either side of the boundaries (see chevron lines in Figure 1), and represents a translation of $\frac{c}{2}[001]$ in the (110) plane. Further, the APBs are found throughout the thin film with a lateral density of about 0.2 APB nm^{-1}. While interface misfit dislocations are observed, marked with the arrows in Figure 1a,b, they do not correlate with APB formation. Misfit dislocations and the relaxed in-plane lattice parameter indicate that the formation of APBs is not directly related to relaxation of strain, but rather the selection of the growth plane based on the mismatch of the film with the STO substrate.

Unlike APBs in cubic perovskites, such as $SrTiO_3$, the APB defects seen here do not arise from off-stoichiometry in the film. The boundaries are generated by a half-unit-cell translation along the doubled pseudocubic unit cell direction, [001], and hence stoichiometry is maintained. Furthermore, the APBs do not correlate with substrate surface steps and the YFO d_{002} spacing is nearly that of STO, with a –2.7% lattice mismatch. Thus, an APB would not be required to accommodate steps on the $SrTiO_3$ surface.[14] Moreover, the APBs are found throughout the film at random positions. Only vertical APBs are found in the films, which originate at the film/substrate interface. Thus the density of such planar defects is not strongly affected by sample thickness. Instead, the density control is primarily governed by the thin film nucleation and growth rate. For example, a previous YFO thin film growth study[4] showed that

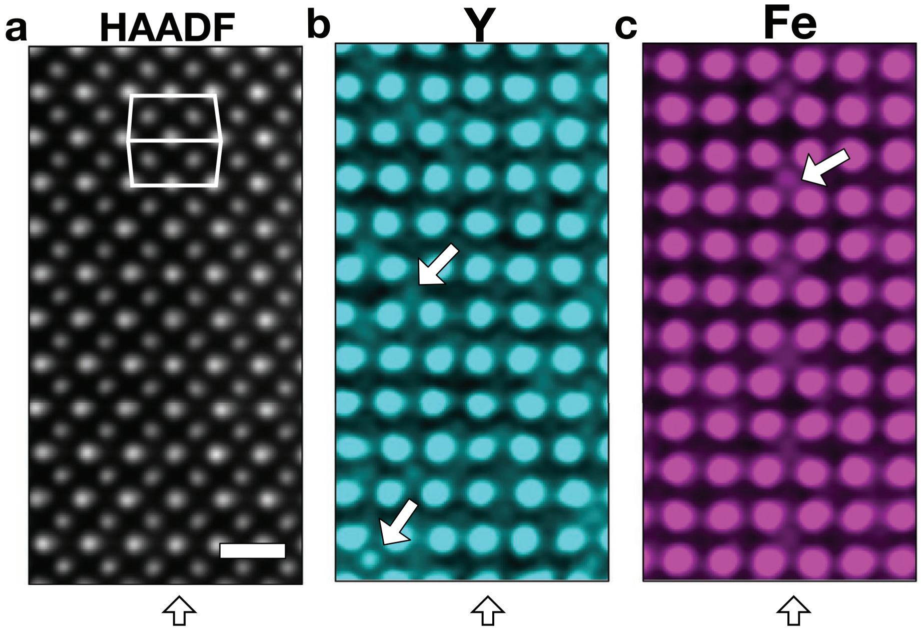

Figure 2. a) HAADF STEM of an (110) antiphase boundary in YFO and corresponding b) Y and c) Fe STEM EDS maps. The scalebar represents 500 pm. The arrows in (b) and (c) point to atom columns containing Y_{Fe} and Fe_Y antisites, respectively.

vertical planar defects initiated at the YFO/STO interface and extended through even a 800 nm thick film.

Further, nucleation of YFO starting on either $(001)_{YFO}$ or $(002)_{YFO}$ exhibits the lowest mismatch relative to STO. Specifically, growth on $\{110\}_{YFO}$ would require the accommodation of –2.7% strain compared to –1.6% for $\{001\}_{YFO}$ (Figure 1d). In addition, the $(001)_{YFO}$ and $(002)_{YFO}$ nuclei can be equivalently initiated on the STO substrate surface where only the Fe-oxygen octahedral tilts are different in the first Fe–O layer of YFO, as shown in Figure 1c. Thus, the vertical APBs in the YFO thin film are the product of coalescence of regions nucleated on $(00L)_{YFO}$ type planes during PLD.

High-angle ADF (HAADF) and atomic resolution EDS confirm that the APBs are nominally composed of Y, as shown in **Figure 2**a,b and expected from the formation mechanism. Further, the Y EDS map shows that Y_{Fe} antisites form throughout the film, as previously reported in Ref. [3]. These antisites have been identified as being responsible for the ferroelectric behavior measured in these Y-rich films. The Fe EDS map, on the other hand, shows that Fe_Y reside at the APB, as in Figure 2c. Further, they are placed at every other Y atom column in the APB. This observation strongly suggests that while the formation energy of Fe_Y antisites is high in 'bulk',[3] it is significantly decreased at the APBs. The background subtracted Fe signal from EDS at the Y sub-lattice on APB suggests that an average of about 10% of Y atoms are replaced by Fe atoms. In a 10 nm thick TEM sample, this represents roughly 2–3 Y atoms replaced by Fe. This contrasts with a previous report of APBs in the orthomanganite $TbMnO_3$, where Mn replaced all (or nearly all) Tb and created a new 2D phase[15]. Also, no significant change in oxygen content is observed at the APBs based on the intensity of oxygen atom columns in the dDPC images as shown in Figure 1c and X-ray absorption spectroscopy (XAS) measurements show that Y and Fe are in 3+ charge states,[3] consistent with oxygen stoichiometry.

To further explore the APBs, structural relaxations at the boundary are measured. The nearest-like-neighbor (NLN) distances for Y are shown in **Figure 3**a. Notably, the Y atom columns align vertically along $[001]_{YFO}$ at the APB in contrast to the zigzag to either side of the boundary. Furthermore, the in-plane Y–Y NLN distances alternate between expansion and contraction by 15% while the in-plane Fe–Fe NLN distances remain constant across the boundary. In contrast, the out-of-plane NLN distances for Y–Y are unchanged and the Fe–Fe distances alternately expand and contract by 7%. The oxygen atom positions also relax at the boundary, where along [001] the projected oxygen positions move toward the Y atom column within the expanded lattice environment, as shown in Figure 1c. These changes represent a significant departure from the 'pristine' crystal structure, and hence the bonding environment is considerably different at the APB.

The net cation displacements at the APB, measured as the difference between the position of an Fe atom column and the centroid of its four surrounding Y atom columns, reflect the departure from the bulk structure symmetry. The average net cation displacement magnitude in Figure 3c is 9 ± 3 pm at the APB, and only 6 ± 3 pm away from the boundary. The net cation displacements can thus be understood as inversion symmetry breaking that leads to polarization at the APB. From these measurements of the projected structure, the APBs exhibit ferrodistortive displacements, with the largest component of polarization along the in-plane direction.

The combination of polar displacements and the presence of Fe_Y antisites strongly suggests that the properties differ significantly at the APBs. Exploring this further, DFT is used to relax the structure of the APB measured from experiment, which was then used to estimate formation energies and local

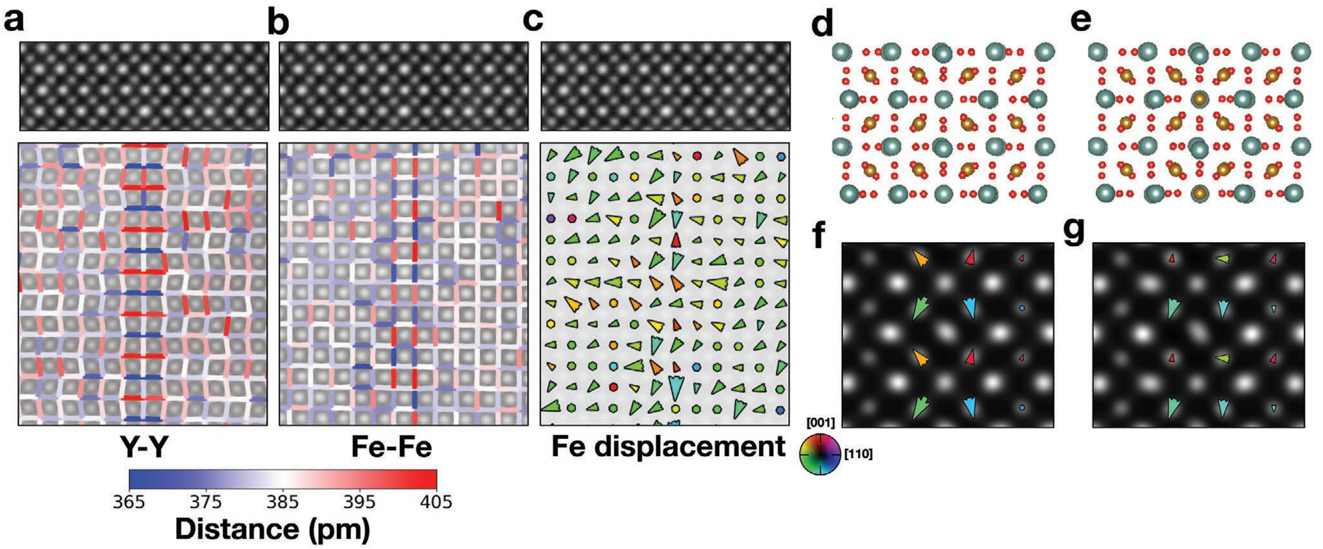

Figure 3. a) Y–Y and b) Fe–Fe NLN distances from ADF STEM. c) The net Fe displacement map obtained from the atom columns positions. d,e) relaxed DFT structure of APB without and with an Fe_Y antisite respectively, f,g) simulated ADF STEM image of APB relaxed DFT structure without and with an Fe_Y antisite, respectively.

polarization with and without Fe antisites, **Figure** 4d,e. To confirm that the DFT APB structure agrees with experiment, ADF STEM images are simulated using relaxed DFT structures, Figure 4f,g. The measured magnitude of the net cation displacement using the simulated APB images is 6 pm with and 9 pm without the Fe_Y antisite, respectively. Furthermore, the Y and Fe sublattices at the APB of the DFT-relaxed structure also expand and contract by 16% (along in-plane) and 8% (along out-plane). The DFT structure is thus in excellent agreement with experiment.

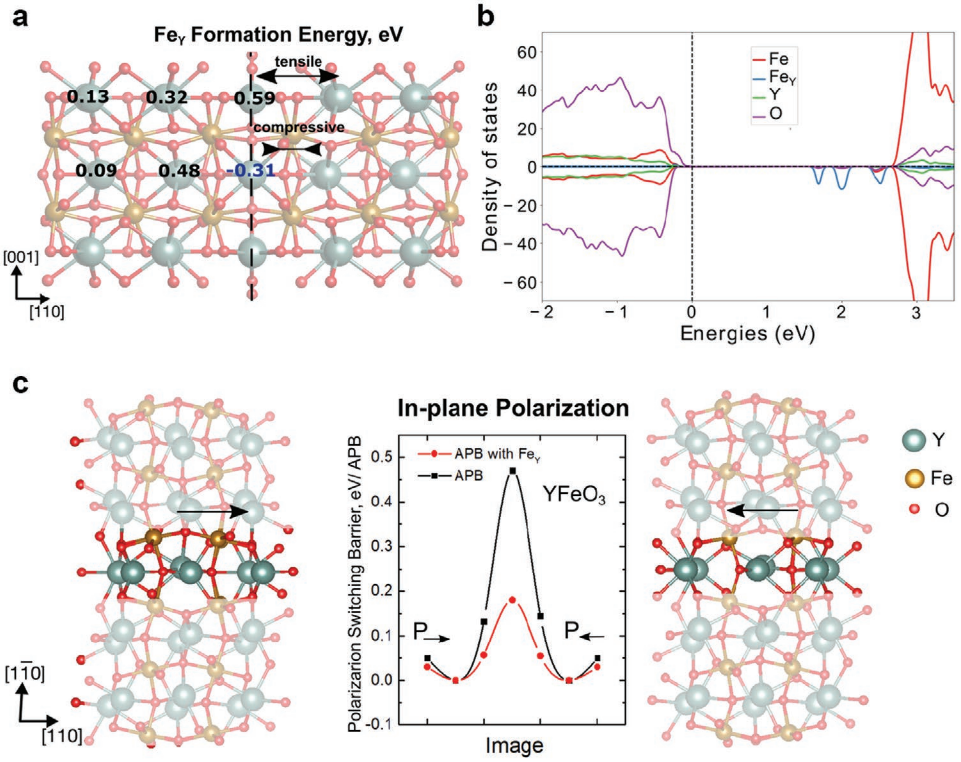

Figure 4. a) The relative formation energies of Fe_Y defects (eV) at different Y positions across an APB. A Fe_Y in bulk YFO was used for the reference energy. b) Projected density of states for Fe-rich APB of YFO where the Fermi level is set to zero. c) DFT calculations demonstrating the bi-stable, polar nature of the (110) APB in YFO.

The formation energy of the observed APBs is found to be 130 mJ m^{-2} from DFT, which is within the range typical for perovskite oxides (100–300 mJ m^{-2}).[18,19] The low boundary formation energy further supports the nucleation and growth model suggested above as the boundaries can form without a large energy penalty. Furthermore, the DFT calculations indicate that the Fe_Y antisites are stabilized by the APBs where the antisite formation energy is decreased (ΔE = –0.31 eV) at the compressive strain locations (see Figure 4a). This is significant as at these Y positions, the Y–O distance is only 2.23 Å compared to 2.29 Å away from the boundary. Thus, the replacement of Y by Fe is favored here because of Fe's smaller ionic radius, which reduces the compressive strain energy. This is in contrast to the Y at APB positions with tensile strain, where a significant increase (ΔE = 0.59 eV) of the Fe_Y formation energy occurs. Furthermore, the DFT calculations also show that while the electronic structure of Fe-rich APB remains insulating, empty states associated with the Fe_Y defects (see Figure 4b) may serve as charge traps and promote p-type conductivity.

As with experiment, in-plane polarization induced by the APBs is also found in the first-principles simulations. The DFT structure shows that in-plane polarization originates from significant off-centering (0.71 Å) of central Y atom at the APB as shown in Figure 4c, which polarizes adjacent layers and causes sizable octahedral distortions. The resulting bi-stable polarization is 19 µC cm^{-2} along $[110]_{YFO}$ with a switching barrier of 0.44 eV/APB. Moreover, bi-stable APBs have also been shown to occur in other perovskite oxides.[19] When Fe_Y antisites are added to the APBs, the off-centering is reduced by more than a factor of three, 0.2 Å, which leads to a decreased ferroelectric polarization of 7.6 µC cm^{-2} (Figure 4c). The smaller displacement along $[110]_{YFO}$ in the DFT relaxed structure is associated with the smaller ionic radius of Fe^{3+} compared to Y^{3+} and ultimately reduces the switching barrier to 0.15 eV/APB. This is significant as a boundary without Fe_Y antisites would exhibit a large switching barrier and could thus act to pin polarization, which can degrade switching behavior. Thus, although the YFO APBs are predicted to exhibit in-plane polarization, their contribution to polarization is reduced by the Fe_Y antisites, and at the density observed here, APB are not the dominant contributor to the measured ferroelectric polarization. Instead, the out-of-plane ferroelectric response remains dominated by the Y_{Fe} antisites.[3]

Beyond the polarization, magnetic properties can be impacted by presence of APBs. In the DFT relaxed structure, the oxygen octahedra at the APBs are found to tilt. This can be observed when viewed normal to $(1\bar{1}0)_{YFO}$, where the separation between the oxygen atom columns decreases at the boundary where tensile strain occurs (inset Figure 1c), which is also observed in experiment as marked by the arrow in Figure 1c. Measured from the DFT structure, the angle between two octahedra along [110] is 140° in centrosymmetric YFO while at the boundary this angle alternates between 139° and 156°. Moreover, the oxygen octahedra at the boundary distort along [001] where the Fe–O distances become asymmetric with a ratio of 1.12. As a consequence of these Fe-O bond angles and distances at the APB, the magnetic properties of the boundary are likely to differ from the rest of the film.[20] For example, superexchange coupling between Fe and O depends on the Fe-O bond distance and angle, which can lead to antiferromagnetic behavior, as seen in $SmFe_xCr_{1-x}O_3$.[20] While the magnetic behavior of these Y-rich YFO thin films measured in experiment show a similar trend to bulk YFO, further increasing the planar defects by controlling the nucleation and growth rate during growth may modify the magnetic response. Thus, these observations point to the need for additional local magnetic property studies of the APBs.

3. Conclusions

The presence of APBs in multiferroic YFO thin films can stabilize Fe_Y antisites, which are otherwise unfavored in the thin film bulk with 20% excess Y. Through direct, atomically-resolved imaging, the APBs exhibit significant structural relaxation of the Y, Fe, and O sub-lattices at the boundary. The combination of STEM measurements with DFT calculations show that the APBs provide a local structural and chemical environment that lowers the formation energy of Fe_Y antisites considerably. The local distortions at the APBs are also shown to be ferrodistortive (in-plane) in nature, which is modified by the presence of Fe_Y defects. Specifically, the bi-stable switching barrier is reduced by a factor of about three, which would reduce, but not eliminate, polarization pinning. While the density of APBs were only occasionally found here, and thus do not strongly influence the measured thin film behavior, further increasing their density via the nucleation rate would tend to pin the polarization in-plane, in addition to introducing additional states within the bandgap. The results thus indicate that APBs can provide an additional means to modify the multiferroic properties of orthoferrites. Finally, we suggest that the mechanism for point defect stabilization by APBs should be common in other functional oxides where the pseudocubic unit cell is doubled along one or more of the crystal axes. In such systems, the APBs may provide a means to locally introduce dopants that would otherwise be unstable in the 'bulk' of the film.

4. Experimental Section

Thin Film Growth: The YFO thin film was grown using pulsed laser deposition on an Nb-doped STO substrate using a KrF excimer laser (λ = 248 nm) with 1.3 J cm^{-2} fluence and 10 Hz repetition rate.[3] A commercial $YFeO_3$ target from Plasmaterials Inc. was used for thin film growth. The substrate was held at 900 °C and the oxygen partial pressure was kept at 10 mTorr. The as-grown thin films were cooled to room temperature under a similar partial pressure of oxygen at a rate of 20 °C min^{-1}.

Scanning Transmission Electron Microscopy: Cross-sectional samples of YFO thin films were prepared for electron microscopy using conventional polishing using an Allied Mulitprep system. A Fischione 1051 argon ion mill was used to thin the samples to electron transparency. Scanning transmission electron microscopy imaging was conducted using a probe-aberration corrected Thermo Fisher Scientific Themis Z G3 S/TEM 60-300kV equipped with an XFEG source operated at 200 kV. The STEM images were acquired with a convergence semi-angle of 18 mrad (ADF) or 25 mrad (dDPC). The images used for structural analysis were acquired using the revolving STEM (RevSTEM) method to ensure image accuracy and precision.[21,22] Each RevSTEM dataset consisted of 20 frames with the fast scan direction rotated 90° between each frame. The atom column locations were extracted from the drift and scan distortion corrected images using a custom Python script.[23]

Atomic resolution EDS data were collected using an Ultra-X detector (>4 strad collection solid angle) equipped on a Thermo Fisher Scientific Spectra Ultra microscope with a X-CFEG source operated at 200 kV. The probe convergence semi-angle was 18 mrad and the electron dose was 4.35×10^3 e^-/pixel. The beam current used during the EDS acquisition (60 pA) was optimized to prevent observable damage to the sample The atomic resolution EDS dataset was processed using non-local principal component analysis to reduce noise and Gaussian blurring via an open-source Matlab script.[24] STEM image simulations were carried out using the multislice approach[25] with imaging conditions from experiment. The simulated sample thickness was 10 nm to match that from experiment determined using position averaged convergent beam electron diffraction.[26] To approximately account for the finite effective source size, simulated images were convolved with an 80 pm full-width at half-maximum Gaussian.[27]

Density Functional Theory: First-principles calculations were performed within density functional theory (DFT) using the projector augmented wave (PAW) potentials[28] as implemented in the Vienna Ab initio Simulation Package (VASP).[29] The generalized gradient approximation Perdew-Burke-Ernzerhof (PBE) exchange-correlation functional[30] was employed with a plane wave cutoff energy of 500 eV. The rotationally invariant PBE + U approach was adopted with $U_{\text{eff}} = 4$ eV on the Fe 3d orbitals. The ions were relaxed by applying a conjugate-gradient algorithm until the Hellmann-Feynman forces were less than 10 meV $Å^{-1}$. In-plane lattice parameters were fixed to simulate epitaxial growth on a cubic $SrTiO_3$ substrate (a = 3.903 Å). Ferroelectric properties were calculated using the Berry-phase approach.[31] Switching barriers were calculated using the Nudged Elastic Band method and electronic structure analysis was carried out using the HSE06 functional.[32] Antiferromagnetic G-type spin-ordering was imposed at the APB.

To implement periodic boundary conditions, a large supercell was considered with two antiphase boundaries along [110] of the Pbnm structure. The resulting supercell was comprised of 8 pseudocubic ABO_3 unit cells along a direction, y, perpendicular to the APB and 2 unit cells along directions x and z parallel to the APB. The APB energy was computed as $E_{\text{APB}} = (E - E_0)/2S$, where E is the total energy of the APB configuration, E_0 the energy of the single-domain supercell of the same size and S is equal to the cross-sectional area of the supercell.

Acknowledgements

J.M.L. and A.K. acknowledge support of this work through the John Chipman Career Development Professorship. A.K. thanks the MIT Mathworks engineering fellowship for support. The DFT calculations were carried out using the Extreme Science and Engineering Discovery Environment (XSEDE),[33] which is supported by National Science Foundation Grant No. ACI1548562. The thin film growth, by S.N and C.A.R, and DFT calculations, by K.K. and B.Y., were supported by the MRSEC Program of the National Science Foundation under award No. DMR-1419807. CAR acknowledges support of SMART, an nCORE Center of the Semiconductor Research Corporation. A NVIDIA Titan Xp GPU used for this research was donated by the NVIDIA Corporation. This work was carried out in part through the use of the MIT Characterization. nano facility.

Conflict of Interest

The authors declare no conflict of interest.

Data Availability Statement

The data that support the findings of this study are available from the corresponding author upon reasonable request.

Keywords

antiphase boundaries, antisite defects, density functional theory, multiferroics, orthoferrites, scanning transmission electron microscopy

Received: July 19, 2021
Revised: October 9, 2021
Published online:

[1] M. Shang, C. Zhang, T. Zhang, L. Yuan, L. Ge, H. Yuan, S. Feng, *Appl. Phys. Lett.* **2013**, *102*, 062903.
[2] M. Shang, C. Wang, Y. Chen, F. Sun, H. Yuan, *Mater. Lett.* **2016**, *175*, 23.
[3] S. Ning, A. Kumar, K. Klyukin, J. H. Kim, T. Su, H.-S. Kim, J. M. LeBeau, B. Yildiz, C. A. Ross, *Nat. Commun.* **2021**, *12*, 4298.
[4] J. Scola, P. Boullay, W. Noun, E. Popova, Y. Dumont, A. Fouchet, N. Keller, *J. Appl. Phys.* **2011**, *110*, 043928.
[5] S. Van Aert, S. Turner, R. Delville, D. Schryvers, G. Van Tendeloo, E. K. Salje, *Adv. Mater.* **2012**, *24*, 523.
[6] D. Morikawa, K. Tsuda, *Appl. Phys. Lett.* **2021**, *118*, 092901.
[7] K. P. McKenna, F. Hofer, D. Gilks, V. K. Lazarov, C. Chen, Z. Wang, Y. Ikuhara, *Nat. Commun.* **2014**, *5*, 5740.
[8] H. M. Yoshio Itoh, M. Yamaguchi, *J. Cryst. Growth* **1990**, *103*, 363.
[9] J. C. Jiang, Y. Lin, C. L. Chen, C. W. Chu, E. I. Meletis, *J. Appl. Phys.* **2002**, *91*, 3188.
[10] F. V. Hensling, H. Du, N. Raab, C. L. Jia, J. Mayer, R. Dittmann, *APL Mater.* **2019**, *7*, 101127.
[11] C. Xu, H. Du, A. J. Van Der Torren, J. Aarts, C. L. Jia, R. Dittmann, *Sci. Rep.* **2016**, *6*, 38296.
[12] M. Luysberg, R. G. Sofin, S. K. Arora, I. V. Shvets, *Phys. Rev. B: Condens. Matter Mater. Phys.* **2009**, *80*, 024111.
[13] Y. Q. Wang, W. S. Liang, P. K. Petrov, N. M. N. Alford, *Appl. Phys. Lett.* **2011**, *98*, 091910.
[14] Z. Wang, H. Guo, S. Shao, M. Saghayezhian, J. Li, R. Fittipaldi, A. Vecchione, P. Siwakoti, Y. Zhu, J. Zhang, E. W. Plummer, *Proc. Natl. Acad. Sci. USA* **2018**, *115*, 9485.
[15] S. Farokhipoor, C. Magén, S. Venkatesan, J. Íñiguez, C. J. Daumont, D. Rubi, E. Snoeck, M. Mostovoy, C. De Graaf, A. Müller, M. Döblinger, C. Scheu, B. Noheda, *Nature* **2014**, *515*, 379.
[16] J. Xi, B. Liu, Y. Zhang, W. J. Weber, *Comput. Mater. Sci.* **2016**, *123*, 131.
[17] P. S. Bharadwaj, S. Kundu, V. S. Kollipara, K. B. Varma, *RSC Adv.* **2020**, *10*, 22183.
[18] P. Hirel, P. Marton, M. Mrovec, C. Elsässer, *Acta Mater.* **2010**, *58*, 6072.
[19] X. K. Wei, A. K. Tagantsev, A. Kvasov, K. Roleder, C. L. Jia, N. Setter, *Nat. Commun.* **2014**, *5*, 3031.
[20] Z. Xiang, W. Li, Y. Cui, *RSC Adv.* **2018**, *8*, 8842.
[21] X. Sang, J. M. LeBeau, *Ultramicroscopy* **2014**, *138*, 28.
[22] J. H. Dycus, J. S. Harris, X. Sang, C. M. Fancher, S. D. Findlay, A. A. Oni, T.-t. E. Chan, C. C. Koch, J. L. Jones, L. J. Allen, D. L. Irving, J. M. LeBeau, *Microsc. Microanal.* **2015**, *21*, 946.
[23] A. Kumar, J. N. Baker, P. C. Bowes, M. J. Cabral, S. Zhang, E. C. Dickey, D. L. Irving, J. M. LeBeau, *Nat. Mater.* **2021**, *20*, 62.
[24] J. Salmon, Z. Harmany, C. A. Deledalle, R. Willett, *J. Math. Imaging Vision* **2014**, *48*, 279.
[25] E. J. Kirkland, *Advanced Computing in Electron Microscopy*, Springer, New York **2010**.
[26] J. M. LeBeau, S. D. Findlay, L. J. Allen, S. Stemmer, *Ultramicroscopy* **2010**, *110*, 118.
[27] J. M. LeBeau, S. D. Findlay, L. J. Allen, S. Stemmer, *Phys. Rev. Lett.* **2008**, *100*, 206101.

[28] P. E. Blöchl, *Phys. Rev. B* **1994**, *50*, 17953.
[29] G. Kresse, J. Furthmüller, *Comput. Mater. Sci.* **1996**, *6*, 15.
[30] J. P. Perdew, K. Burke, M. Ernzerhof, *Phys. Rev. Lett.* **1996**, *77*, 3865.
[31] R. King-Smith, D. Vanderbilt, *Phys. Rev. B* **1993**, *47*, 1651.
[32] A. V. Krukau, O. A. Vydrov, A. F. Izmaylov, G. E. Scuseria, *J. Chem. Phys.* **2006**, *125*, 224106.
[33] J. Towns, T. Cockerill, M. Dahan, I. Foster, K. Gaither, A. Grimshaw, V. Hazlewood, S. Lathrop, D. Lifka, G. D. Peterson, R. Roskies, J. R. Scott, N. Wilkins-Diehr, *Comput. Sci. Eng.* **2014**, *16*, 62.